quantum beam science

MDPI

Article

Advanced Small-Angle Scattering Instrument Available in the Tokyo Area. Time-of-Flight, Small-Angle Neutron Scattering Developed on the iMATERIA Diffractometer at the High Intensity Pulsed Neutron Source J-PARC

Satoshi Koizumi [1,*], Yohei Noda [1], Tomoki Maeda [1], Takumi Inada [1], Satoru Ueda [1], Takako Fujisawa [1], Hideki Izunome [2], Robert A. Robinson [1,3] and Henrich Frielinghaus [4]

1 Institute of Quantum Beam Science, Ibaraki University, 162-1 Shirakata, Tokaimura, Nakagun, Ibaraki 319-1106, Japan; yohei.noda.77@vc.ibaraki.ac.jp (Y.N.); tomoki.maeda.polymer@vc.ibaraki.ac.jp (T.M.); takumi.inada.sans@vc.ibaraki.ac.jp (T.I.); satoru.ueda.fas@vc.ibaraki.ac.jp (S.U.); takako.fujisawa.fas@vc.ibaraki.ac.jp (T.F.); chicoma61@outlook.com (R.A.R.)

2 Hitachi Denki Kogyo Co., Ltd., 1270-17 Tomecho, Hitachi, Ibaraki 319-1231, Japan; izunome@hd-ind.co.jp

3 School of Physics, University of Wollongong, Wollongong 2522, Australia

4 Jülich Center for Neutron Science at MLZ, ForschungsZentrum Jülich GmbH, Lichtenbergstrasse 1, 85747 Garching, Germany; h.frielinghaus@fz-juelich.de

* Correspondence: satoshi.koizumi.prof@vc.ibaraki.ac.jp

Received: 1 August 2020; Accepted: 25 November 2020; Published: 2 December 2020

Abstract: A method of time-of-flight, small-angle neutron scattering (TOF-SANS) has been developed based on the iMATERIA powder diffractometer at BL20, of the Materials and Life Sciences Facility (MLF) at the high-intensity proton accelerator (J-PARC). A large-area detector for SANS, which is composed of triple-layered ^{3}He tube detectors, has a hole at its center in order to release a direct beam behind and to detect ultra-small-angle scattering. As a result, the pulsed-neutron TOF method enables us to perform multiscale observations covering $0.003 < q$ (Å^{-1}) < 40 ($q_{max}/q_{mix} = 1.3 \times 10^4$) and to determine the static structure factor $S(q)$ and/or form factor $P(q)$ under real-time and in-situ conditions. Our challenge, using unique sample accessories of a super-conducting magnet and polarized neutron, is dynamic nuclear polarization (DNP) for contrast variation, especially for industrial use. To reinforce conventional SANS measurements with powder materials, grazing-incidence small-angle neutron scattering (GISANS) or reflectivity is also available on the iMATERIA instrument.

Keywords: multiscale; real-time and in-situ; small-angle scattering; contrast variation; reflectivity

1. Introduction

The softness of materials such as gels, foams and rubber is attributed to the reorganization of self-assembled molecular structures [1]. The interaction energy to associate molecules (hydrogen bonding, van der Waals or hydrophobic interactions) is of the order of the thermal energy at room temperature (~k_BT). Furthermore, molecules comprising soft materials possess a large amount of internal degrees of freedom. Consequently, soft materials react in a viscoelastic manner to external stimuli such as deformation (stretching or shear), and/or temperature or pressure jumps. The taste and texture of foods, the softness of clothes, and the fuel efficiency and stopping performance of tires, are all related to viscoelasticity coupled with the hierarchical structure. Time-of-flight (TOF) neutron

scattering, as reported in this paper, is an experimental method to delicately and instantaneously detect the hierarchical structure over a wide range from mesoscopic to microscopic atomic scales.

Neutron scattering is an indispensable analytical tool for materials science investigations [2]. Especially, small-angle neutron scattering (SANS) is powerful in performing quantitative, nondestructive and in-situ observations in reciprocal space not only on domain structures, but also on concentration fluctuations and gradients at interfaces [3], which are not visible by electron microscopy. SANS does not require any special preparation treatments, such as freezing, cutting and staining, which are necessary for electron microscopy. Tissues in living cells (such as mesh, layer and bundle) are also a target of SANS observation. When we look at the cell (schematically shown in Figure 1 in [4] its size ranges from 100 nm to several nm and it is filled with organelles (nucleolus, mitochondria, chloroplasts, endoplasmic reticulum, etc.), the size of which are about 1 μm~100 nm. The cell and its organelles are enclosed by a plasma membrane (~nm), which is composed of lipids. In a membrane or cytoplasm, there are a huge number of proteins, acting as channels, enzymes, the cytoskeleton, etc. Figure 1 shows a schematic diagram of various hierarchical structures, which we can find in materials or life. Interestingly, we notice that the living cells appear from the length scales of 100 nm. To access this hierarchical self-assembly found in nature, we need to cover a wide range of length scales from Ångstroms to μm.

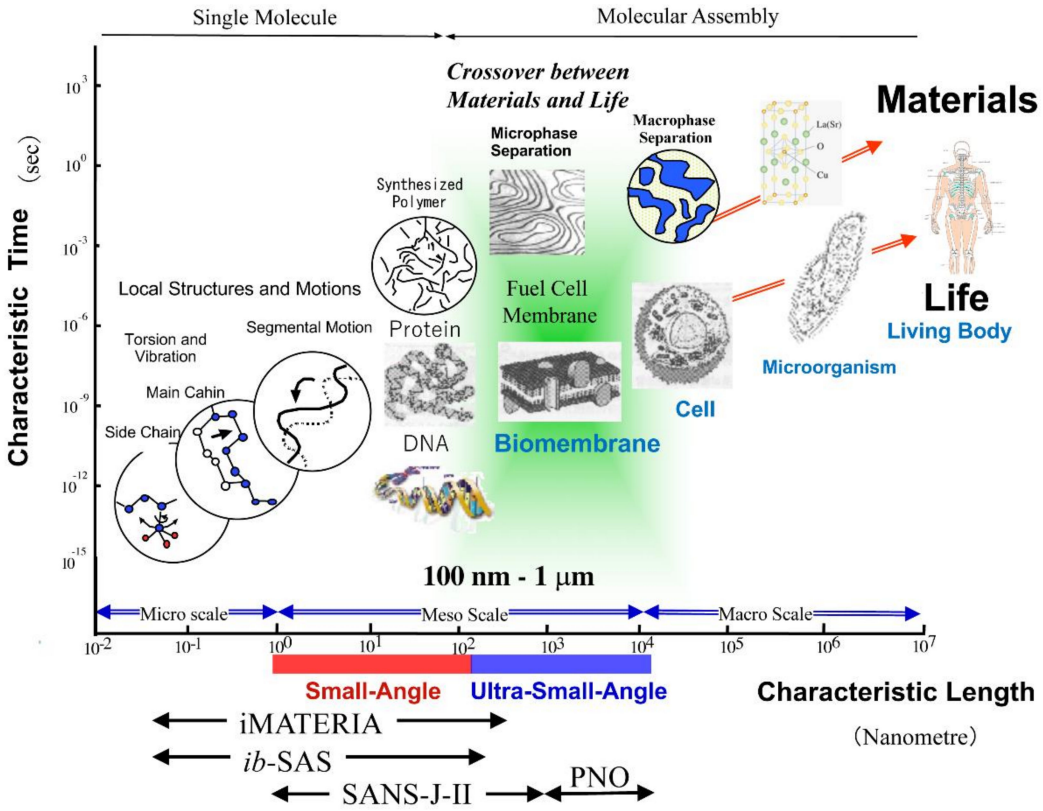

Figure 1. Schematic diagram of hierarchical structures describing materials and life appearing from atomic to macroscopic scales. The length scales covered by small-angle neutron scattering spectrometers in the Tokyo area are indicated.

SANS instruments across the world have been developed considering the type of neutron sources (reactor or accelerator) [3]. Research reactors with a continuous neutron beam are advantageous for large-scale observation by achieving the smallest accessible wave number $q_{\min}$. A focusing ultra-small-angle, neutron-scattering method was recently developed by using a monochromatic beam and focusing lenses [3,4]. The refractive lens [5,6] or magnetic lens [7] was invented in around 2000 and is combined with a small area detector with a higher spatial resolution of mm. The focusing method

covers the q-region down to 10^{-4} Å^{-1} and reinforces a Bonse–Hart double-crystal method using perfect crystals [8,9], which covers the q-region down to 10^{-5} Å^{-1} [3,4]. For example, at the research reactor JRR-3, the focusing SANS instrument (SANS-J-II) [3,4] and double-crystal, ultra-small-angle scattering (USANS) instrument (PNO) [10] are combined complementarily. The focusing method is standard as an option on pin-hole SANS instruments all over the world [11–16]. Hierarchical structures, appearing in various types of soft matter, have been explored by combining SANS and USANS instruments at the JRR-3 reactor, Japan [17–20].

A proton accelerator, providing pulsed neutrons, is advantageous if one wishes to extend the q-region wider, achieving an accessible maximum wave number $q_{\max}$. A time-of-flight (TOF) method does not require monochromation and minimizes the loss of incident neutrons [21,22]. A wide range of length scales is covered from atomic to meso scales. Even at reactors, the incident beam can be chopped as a pulse, in order to achieve $q_{\max}/q_{\mathrm{mix}} = 1000$ [23,24]. Time-of-flight or wavelength dispersion has the merit of avoiding angular scanning, for changing q of reflectivity or double crystal USANS [25,26]. Recently compact pulse sources have become available. The *ib*-SAS instrument, using a TOF method with pulsed neutrons, was prepared as a RANS compact neutron source at RIKEN, Wako Japan [27,28].

In this paper, we report on recent developments and the current status of time-of-flight SANS on the iMATERIA diffractometer at the Japan Proton Accelerator Research Complex (J-PARC). The available wavelength is ranged from 1 to 10 Å, when we choose double-frame chopper operation. Consequently, we achieved multiscale observations covering $0.003 < q$ (Å^{-1}) < 40 ($q_{\max}/q_{\mathrm{mix}} = 1.3 \times 10^4$). A new area detector for SANS was installed, in order to provide access for USANS in the future [29]. Reflectivity is also available to assess fine structures on a solid surface [30,31]. Our big challenge at BL20 is to achieve contrast variation by dynamic nuclear polarization (DNP); both the neutron beam and hydrogen (in the specimen) are polarized in order to tune the coherent scattering length density for contrast variation. The DNP apparatus at the iMATERIA diffractometer is already open for industrial use [32]. There are a variety of SANS instruments achieved currently, which are listed in the introduction [8–28]. In this paper, we intend to indicate a new benchmark of advanced SANS apparatus for the next generation.

2. iMATERIA Spectrometer

At the Japan Proton Accelerator Research Complex (J-PARC), three MeV protons hit a mercury target with a pulse repetition frequency of 25 Hz. In the Materials and Life Sciences Facility, (MLF), there are 23 beam lines in two beam halls, and the iMATERIA diffractometer is located at BL20 (Figure 2), facing towards a poisoned decoupled moderator producing a narrow pulse width of ~10 μs. Neutrons are transported by a supermirror (3 θ_c) guide. Along the beam line, there are three disk choppers (at 7.5, 11.25 and 18.75 m) and a T_0 chopper (10 m) in order to shape the neutron pulse in time. The supermirror guide after the disk chopper 2 is 11.75 m long and 34×34 mm^2 in cross-section. Upstream of the instrument (part A in Figure 2), a polarizing supermirror, π-flipper and multipinhole collimator have been installed [32], to make finer collimation possible for USANS. At the downstream of the instrument (part B in Figure 2), we will install a USANS detector in the future.

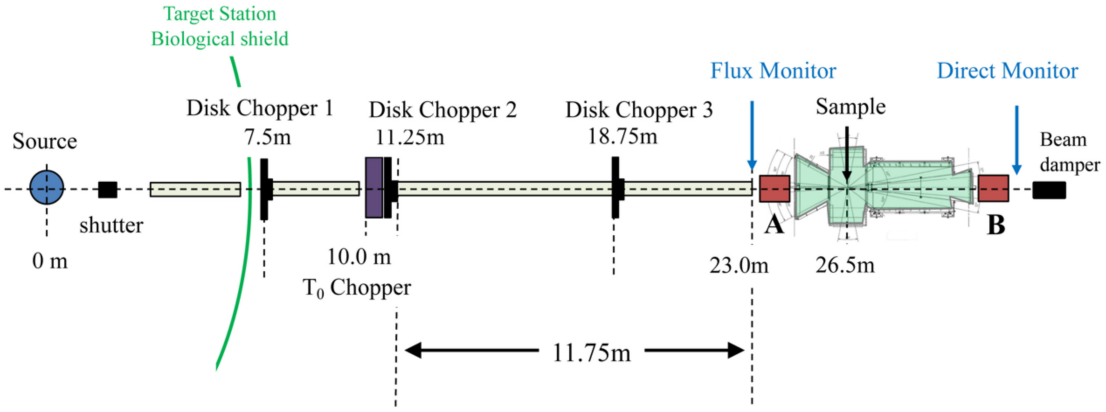

Figure 2. Schematic diagram of BL20 beam line. Upstream of the iMATERIA spectrometer, as indicated by A, new collimation, a polarizing mirror and p-flipper have been installed. Downstream at B, a USANS detector is under development.

Figure 3a shows a schematic diagram of the iMATERIA diffractometer (BL20), which is dedicated to industrial use. The iMATERIA diffractometer was originally designed for powder diffraction, and its original design before reconstruction for SANS is described in [33]. Four detector blocks—(1) small-angle (SA; $0.5 < 2\,\theta < 5.5°$), (2) low-angle (LA; $10 < 2\,\theta < 40°$), (3) 90 degree (SE; $80 < 2\,\theta < 100°$) and (4) backscattering (BS; $150 < 2\,\theta < 175°$)—surround the sample position and cover a wide $2\,\theta$ range (0.1°–180°). Figure 3b shows the 3-dimensional layout of the ^{3}He detectors, the total number of which is about 1500. The view from sample position downstream is towards the small-angle detectors in the center and a six-fold array of low-angle detectors covering the forward-scattering path.

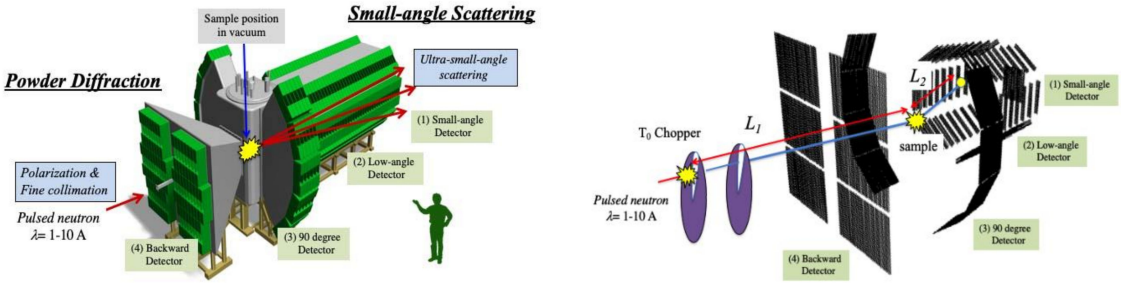

(**a**) (**b**)

Figure 3. (**a**) Schematic diagram of the iMATERIA diffractometer (BL20) at the Materials and Life Sciences Facility (MLF) at the high-intensity proton accelerator (J-PARC), Tokyo. (**b**) Schematic view of tube detectors of the iMATERIA diffractometer, covering the sample position and tube detectors, highlighting the small-angle and low-angle detector blocks.

Since 2016, the large-area detector for SANS has been refurbished [28] and the instrument started its User program. The details of the large-area detector are described in [29]. Figure 4a shows a photo of the large area detector, composed of ^{3}He linear position-sensitive detectors. With a three-layered structure (Figure 4b), we prepared a hole at the center (100×100 mm^2), in order to release the direct (unscattered) neutron beam. Behind the small-angle detector as shown by B in Figure 2, we installed an additional chamber containing the ^{3}He direct beam monitor and USANS detectors (Figure 4c). With the USANS apparatus, we aim to access up to 10^{-4} Å^{-1}, in the near future. As a result, the versatile combination of SANS and powder diffraction is characteristic for wide q observation with high resolutions. By combining wide range of scattering angle ($2\,\theta$) and a wide band of wave length

(λ = 1–10 Å), (combination of scattering-angle-dispersive and wavelength -dispersive methods), a wide q-region (from 0.003 to 40 Å^{-1}, implying $q_{max}/q_{mix} = 1.3 \times 10^4$) can be immediately covered.

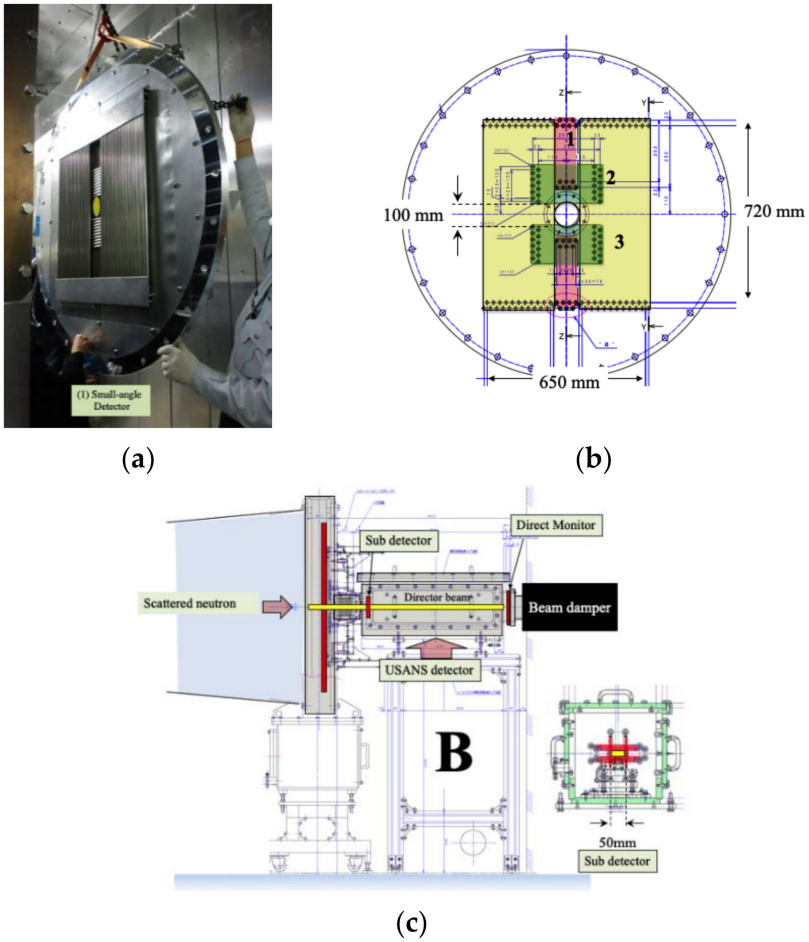

Figure 4. (**a**) Photo of the new small-angle scattering detector. (**b**) Three-layered allocation of tube detectors as indicated by numbers (1, 2 and 3), in order to introduce a hole at the center. (**c**) Ultra-small-angle scattering detector is developed behind the main small-angle scattering detector, as indicated by B (corresponding to B in Figure 2).

3. Scattering Law and Data Reduction

3.1. Time-of-Flight Scattering Method

Figure 5 shows a schematic diagram showing scattering geometry (incident and scattered neutron with wave number 2 π/λ and scattering angle 2 θ). The orthogonal coordinate is defined with the z-axis parallel to the incident beam, and x- and y-axes parallel to the surface of the small-angle detector. A scattering process is described by scattering vector $\vec{q}$. For glassy materials or a solution with slow dynamics, we postulate elastic scattering wave number k for the incident and scattered beam, $\left|\vec{k}_f\right| \cong \left|\vec{k}_i\right| = \frac{2\pi}{\lambda}$.

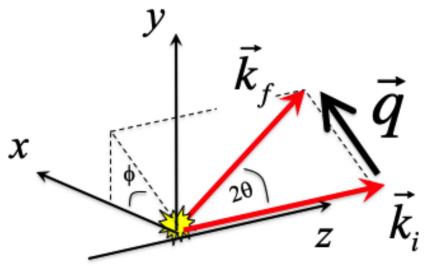

Figure 5. Scattering geometry and definition of scattering wave number q.

Therefore, we obtain

$$q = \left|\vec{q}\right| = \frac{4\pi}{\lambda}\sin\theta, \tag{1}$$

where λ is a wavelength and 2 θ is the scattering angle. For incident and scattered beams, in orthogonal coordinates,

$$\vec{k_i} = \frac{2\pi}{\lambda}(0,\ 0,\ 1) \text{ and } \vec{k_f} = \frac{2\pi}{\lambda}\left(\frac{x}{L_2},\ \frac{y}{L_2},\ \frac{z}{L_2}\right), \tag{2}$$

where L_2 is a distance from sample to detector, as defined in Figure 3b. We redefine $\vec{q}$ as

$$\vec{q} = \left(q_x, q_y, q_z\right) = \frac{2\pi}{\lambda}\left(\frac{-x}{L_2},\ \frac{-y}{L_2}, 1 - \frac{z}{L_2}\right), \tag{3}$$

or with polar coordinates

$$\vec{q} = \frac{4\pi\sin\theta}{\lambda}\left(-\cos\theta\cos\phi, -\cos\theta\sin\phi, \sin\theta\right), \tag{4}$$

where ϕ is an azimuthal angle, defined in the x–y plane.

The neutron is a fundamental particle with mass ($m_n = 1.675 \times 10^{-27}$ kg) and spin ($P_n = \pm 1/2$). According to a textbook of quantum mechanics and wave-particle duality therein, the neutron wavelength is given by the de Broglie principle with Plank's constant h,

$$\lambda = \frac{h}{p} \tag{5}$$

where p is momentum given with mass and velocity v, as $p = m_n v$. With a traveling distance and time, L and t_{TOF}, velocity is given as $v = \left(\frac{L}{t_{TOF}}\right)$. Therefore, we obtain

$$\lambda = \left(\frac{ht_{TOF}}{m_n L}\right). \tag{6}$$

For scanning q, there are two methods: (i) angular-dispersive method—by changing a scattering angle 2 θ (usually detector positions with respect to the beam), q values are scanned. For SANS at a reactor source, we usually change detector positions away from the sample position with using continuous and monochromatic neutrons, and (ii) wavelength-dispersive method—for SANS at a spallation source, q values are usually scanned by using the time-of-flight method using highly intensified nonmonochromatic neutrons. Note that even at a spallation source with the pulsed neutrons or at a reactor source [23,24], the combination of (i) and (ii) is more effective to widely scan q. To elucidate hierarchical structure, many orders of magnitude in q should be covered as much as possible. Toward wider q, the wavelength-dispersive method at a pulsed neutron source profits by gaining q_{max} and therefore q_{max}/q_{min}. Toward smaller q, on the other hand, the wavelength-dispersive method is no longer necessary because the smallest q is obtained by a combination of the smallest θ

and longest λ. Therefore, pin-hole SANS (not a perfect crystal type) is preferable for achieving the smallest $q_{\min}$ by avoiding frame-overlap of pulsed neutrons.

3.2. Data Reduction for Plate Shape Sample

Figure 6 shows a data reduction program of SANS at the iMATERIA spectrometer, treating time-of-flight event data, which converts the real space image to a reciprocal space image by considering Equations (1)–(6), (parts ④ and ⑤ in Figure 6). By selecting a narrow band of wavelengths, users can examine the scattering as a monochromatic beam experiment like at reactor (part ② in Figure 6). According to Equations (1)–(6), from event data with a flight time t_{TOF}, q-value is determined. By circularly averaging or sector averaging over an azimuthal angle φ (part ③ in Figure 6), the scattering profile $I^s_{obs}(\lambda, \theta)$ can be obtained. The data-reduction program can also be applied to reflectivity measurements, which will be discussed in Section 5.2.3. The measured intensity $I^s_{obs}(\lambda, \theta)$ is given with background scattering $I^{bck}_{obs}(\lambda, \theta)$ as follows:

$$I^s_{obs}(\lambda, \theta) = I_0(\lambda) K_I A_s D_s \frac{d\sum^s}{d\Omega}(\lambda, \theta)\, T_r{}^s(\lambda)\, \eta(\lambda)\, \Delta\Omega + I^{bck}_{obs}(\lambda, \theta) T_r{}^s(\lambda) \tag{7}$$

where $\frac{d\Sigma}{d\Omega}(q)$ is the differential scattering cross-section.

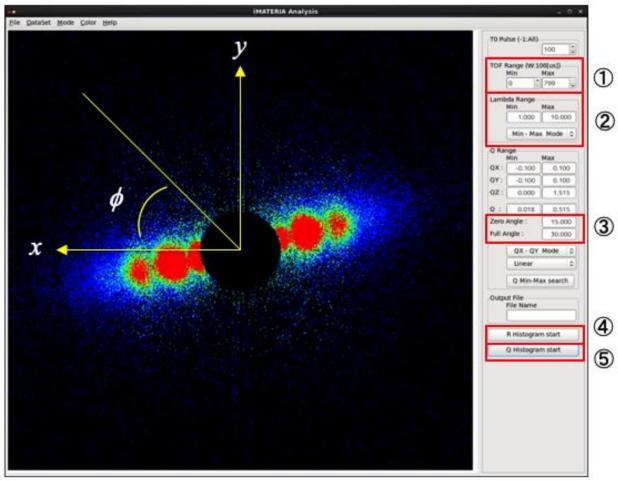

Figure 6. User interface of data reduction program for iMATERIA, showing small-angle neutron scattering (SANS) obtained for a lamellar block copolymer film.

Note that $I^s_{obs}(\lambda, \theta)$ is proportional to the incident beam intensity $I_0(\lambda)$, sample volume ($A_S D_S$) and transmission $T_r{}^s(\lambda)$, where A_S and D_S is sample cross-section and thickness. K_I is an instrument constant. $\eta(\lambda)$ and $\Delta\Omega$ are counting efficiency and the solid angle of a detector element. Therefore, we obtain

$$\frac{d\sum^s}{d\Omega}(\lambda, \theta) = \left[\frac{I^s_{obs}(\lambda, \theta)}{T_r{}^s(\lambda)} - I^{bck}_{obs}(\lambda, \theta)\right] / [I_0(\lambda) N\, \eta(\lambda) \Delta\Omega]. \tag{8}$$

Note that $I_0(\lambda)$, $T_r{}^s(\lambda)$ and $\eta(\lambda)$ are wavelength-dependent. We define a distance as $L = L_1 + L_2$, which is a sum of L_1 (from T_0 chopper to a sample) and L_2 (from a sample to detector). An absolute intensity unit (cm^{-1}) is obtained by considering SANS for a secondary standard of glassy carbon [29].

With the neutron counts from a direct beam monitor behind a small-angle scattering detector, neutron transmission $T_r{}^s(\lambda)$ is calculated as follows:

$$T_r{}^s(\lambda) = \left[I^s_1(\lambda) - I^{close}_1(\lambda)\right] / \left[I^{bck}_1(\lambda) - I^{close}_1(\lambda)\right] = \exp(-\Sigma_T D_s), \tag{9}$$

where $I_1^s(\lambda)$, $I_1^{bck}(\lambda)$ and $I_1^{close}(\lambda)$ are the transmitted beam intensity for the sample, background and beam-close measurements, respectively. The beam-close measurement is conducted by putting B_4C block at the sample position. D_s is thickness of the sample. Σ_T is macroscopic total cross-section, composed of scattering Σ_S, incoherent scattering cross-section (Σ_{inc}) and absorption cross-section Σ_A, as follows:

$$\Sigma_T = \Sigma_S + \Sigma_{inc} + \Sigma_A. \tag{10}$$

Using coherent and incoherent scattering and absorption microscopic cross-sections (σ_{coh}, σ_{inc}, and σ_{abs}, respectively), Σ_T is given by $\Sigma_T = n(\sigma_{coh} + \sigma_{inc} + \sigma_{abs})$, where n is number density as defined n=N/V. Microscopic scattering cross-sections are given by $\sigma_{coh} = 4\pi b_{coh}^2$ and $\sigma_{inc} = 4\pi b_{inc}^2$, where b_{coh} and b_{inc} are coherent and incoherent scattering lengths. Note that a mean free path (MFP) is given by MFP = $1/\Sigma_T$.

Differential scattering cross-section $\frac{d\Sigma}{d\Omega}(q)$ is given by

$$\frac{d\Sigma}{d\Omega}(q) = \sum_i \sum_j b_i \exp\left(\vec{q}\vec{r_i}\right) b_j \exp\left(-\vec{q}\vec{r_j}\right) \tag{11}$$

b_j is coherent scattering length density for i-component and $\vec{r_{ij}}$ $(= \vec{r_j} - \vec{r_i})$ is a vector between i-th and j-th atoms. Phase difference in path between the neutrons scattered by i-th and j-th atoms is given as $\Delta L = -\vec{q} \cdot \vec{r_{ij}}$. Normal SANS usually observes an isotropic and random-oriented powder or solution. In this limit, the golden equation by Debye [34], is obtained as follows:

$$\frac{d\Sigma}{d\Omega}(q) \sim \sum_{i,j} b_i b_j \exp\left(-\vec{r_{ij}} \cdot \vec{q}\right)_\Theta \tag{12}$$

Then it becomes

$$\frac{d\Sigma}{d\Omega}(q) \sim \sum_{i,j} b_i b_j \frac{\sin\left(qr_{ij}\right)}{\left(qr_{ij}\right)} \tag{13}$$

where Θ is an angle between a scattering vector and principle axis of the scattering object. After random-averaging in Θ for isotropic systems, q is given as scalar. Because of random-averaging in Θ, limited special resolution accessible by SANS does not allow the study of local ordered structures, for example, contact ionomers on a fuel cell catalyst. To address this issue, the option of simultaneous use of reflectivity (RF) technique is available on the iMATERIA (see Section 5.2.3 for more details). Our data reduction program in Figure 6 is also available for obtaining RF profiles. It should be strongly emphasized that our measurable SANS is determined simply by varying q and b, according to Equation (13), in relation to materials we are interested in.

4. Sample Environment

The sample position of the iMATERIA diffractometer is in vacuum and 0.6 m below the floor of the standing stage for users. In order to handle a sample specimen for SANS measurements, we prepared an elevator stage with a 4-fold slit with sintered B_4C plates with a tapered edge (Figure 7a,b). Figure 7c is a top view of the stage: it is sustained by four poles which do not block the scattering toward four detector blocks from small-angle to backward scattering. On the stage, we can change between different sample environments, e.g., a temperature-controlled sample stage (25~200 °C) with five sample positions. Figure 7d shows the sample stage kept in air. Figure 8 shows the auto-sample changer for round-shaped specimens operated at room temperature (no temperature control); 40 cuvettes automatically are moved to the beam position. The elevator stage in an air chamber is also available, which is used for in-situ grazing-incidence scattering (GISANS) observation of polymer electrolyte fuel cells under operation, as discussed below in Sections 5.2.3 and 5.2.4. Figure 9 shows the gonio-stage for GISANS and reflectivity available on a sample stage ((b) horizontal and (c) vertical goniometer

stages, respectively). It is shielded in an atmosphere environment container (Figure 9a). Temperature is controlled by heaters. To control the substrate angle relative to the incident beam, a rotary goniometer stage is used. As an extreme condition measurement, dynamic nuclear polarization (DNP) with a super-conducting magnet, with ^{4}He cooler, is also available on iMATERIA (see Section 5.2.5).

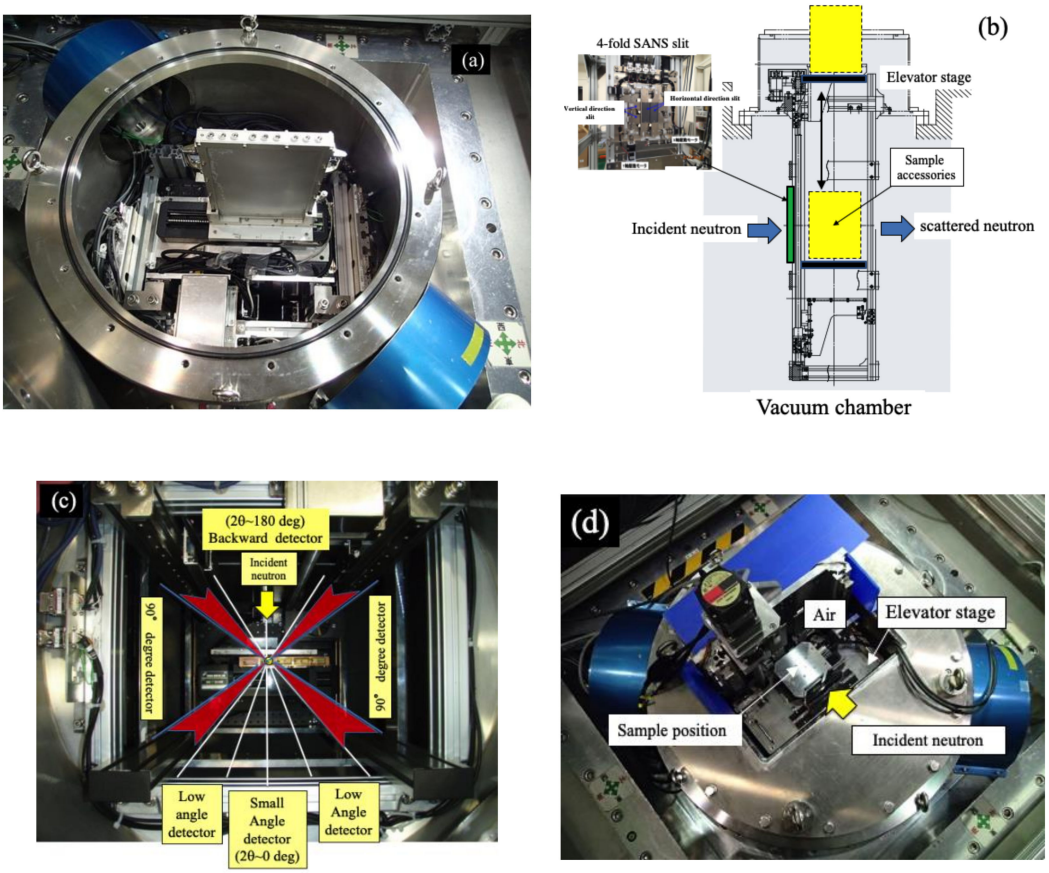

Figure 7. iMATERIA's sample stage: (**a**) photo of in-vacuum components; (**b**) schematic diagram; (**c**) top view; (**d**) photo of top flange and components in air.

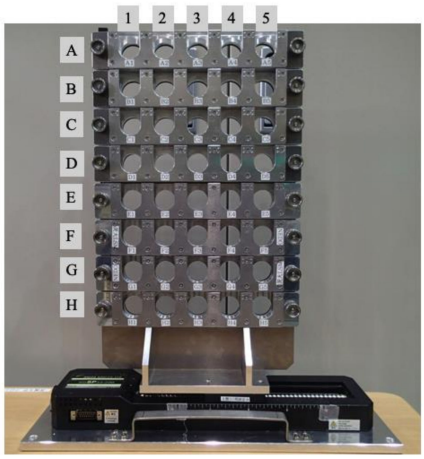

Figure 8. Standard sample changer (40 cuvettes for a round-shape specimen).

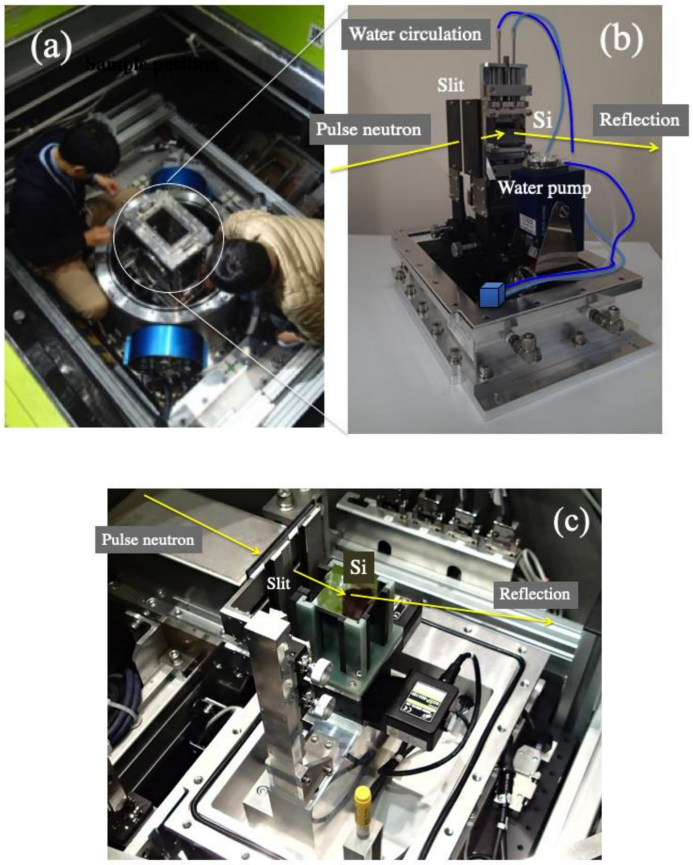

Figure 9. (**a**) Air chamber for grazing-incidence scattering. (**b**) Sample stage for grazing incidence scattering (vertical geometry). (**c**) Sample stage for grazing incidence scattering (horizontal geometry).

5. Results

5.1. Measurements for Calibration

5.1.1. Incoherent Scattering of Vanadium

Figure 10a shows incoherent scattering from a vanadium standard specimen, calibrated for counting efficiency for different wavelengths. The different colors indicate the incoherent scattering obtained with different wavelengths λ from 1 to 10 Å. Figure 10b shows $I_0(\lambda)$, obtained for double-frame (12.5 Hz) operation. After calibration of $I_0(\lambda)$, the scattering obtained for individual wavelengths λ is normalized in order to have q-independent incoherent scattering, as shown in Figure 10a. The determined calibration factor $\eta(\lambda)$ is shown in Figure 10c,

$$\eta(\lambda) = 0.98 \exp(0.52 \times \lambda) + 0.02 \tag{14}$$

which is used for data reduction according to Equations (7)–(9).

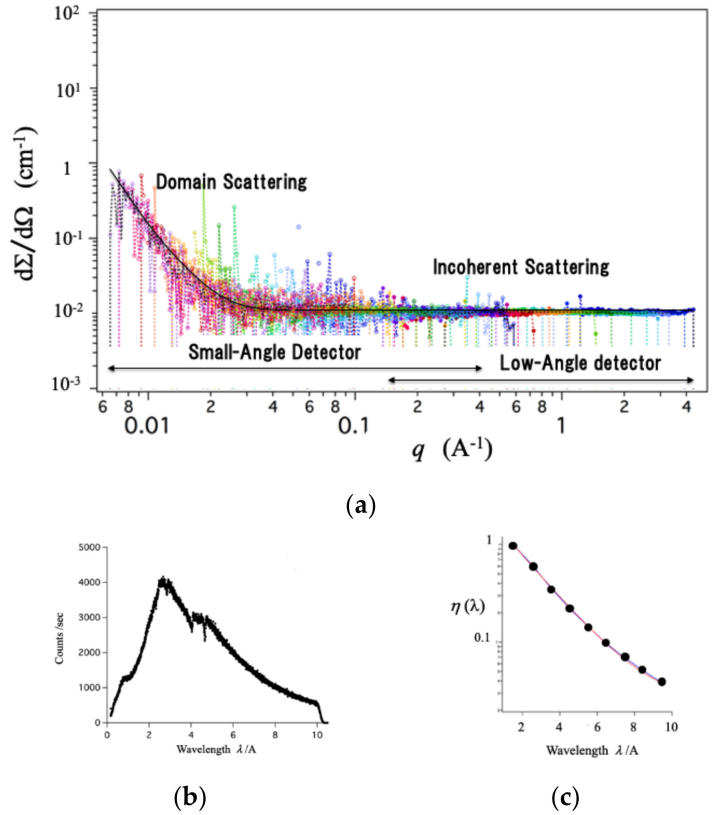

Figure 10. (**a**) Incoherent scattering obtained for vanadium standard sample, using small-angle and low-angle detectors. The different colors indicate the incoherent scattering obtained with different wavelength λ from 1 to 10 Å. (**b**) Incident flux of BL20 as a function of wavelength λ. (**c**) Counting efficiency as a function of wavelength, as determined by scattering from the vanadium standard sample.

5.1.2. Mesoporous Silica

Figure 11a shows the result obtained for a powder of mesoporous silica (TMPS 2.7 mm), showing the q-region covered by a single shot measurement simultaneously using the forward detectors (small-angle, low angle detector and partially-ultra-small-angle scattering blocks) (0.003–4 $Å^{-1}$). It should be stressed that the minimum observable wave number q_{min} = 0.003 A^{-1}. When we access down to q_{min} = 0.003 $Å^{-1}$, we then use a USANS detector and insert fine collimation upstream of the sample ($\delta\theta$ = 0.004 rad for both vertical and horizontal directions).

Figure 11b shows the wavelength-dependent transmissions ($T_r^s(\lambda)$) obtained for the mesoporous silica (TMPS-2.7 mm). According to Equations (9) and (10), $T_r^s(\lambda)$, which varies from 1.0 to 0.8 as increasing λ, is given by incident beam intensity ($I_0^s(\lambda)$ and $I_0(\lambda)$). Absorption cross-section depends on wavelength λ.

$$\Sigma_T = n\left(\sigma_s + \frac{\lambda}{1.8}\sigma_{abs}\right) \quad (15)$$

Note that σ_{abs} is determined for thermal neutrons of λ = 1.8 Å. The gradual decrease in $T_r^s(\lambda)$ is attributed to neutron absorption and diffraction.

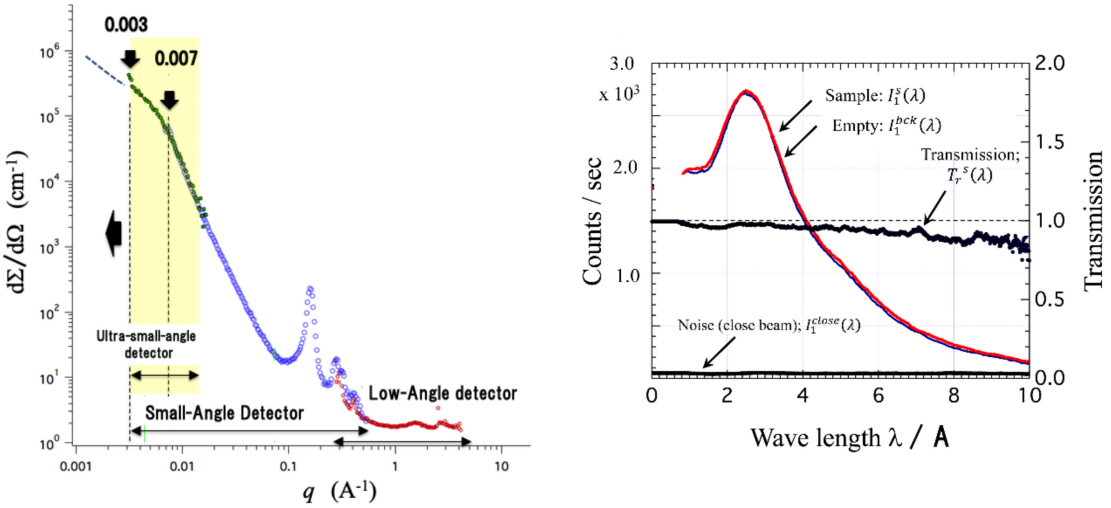

Figure 11. (**a**) Scattering obtained for a powder of mesoporous silica, showing q-region covered by the ultra-small-angle (green), small-angle (blue) and low-angle (red) detector blocks. (**b**) Transmission for powder of mesoporous silica, as a function of λ.

5.1.3. Mono-Disperse Microspheres (SiO_2)

In order to examine q-resolution, we measured SANS on SiO_2 microspheres, as shown in Figure 12. The scattering profile (red in Figure 12) was obtained by a single shot measurement simultaneously using the forward detectors (small-angle and low-angle detector blocks). The scattering function for a spherical object is given by a form factor $P(q)$ and a structure factor $S(q)$,

$$\frac{d\Sigma}{d\Omega}(q) = \Delta b^2 n_p V_p^2 P(q) S(q) \tag{16}$$

where n_p and V_p^2 are number density and volume of a sphere. Δb is a contrast as defined, $\Delta b = b_j - b_i$. Note that in case of air, $b_i = 0$. The difference in scattering length density, the form factor $P(q)$ of sphere with a radius R is given by,

$$P(q) = \frac{[\sin(qR) - qR\cos(qR)]^2}{(qR)^6} \tag{17}$$

When there is polydispersity in size R, the averaged scattering is given by

$$\hat{P}(q) = C \int_{R_{min}}^{R_{max}} \exp\left[-(R - R_{AV})^2 / 2\sigma_R\right] P(q, R) dR \tag{18}$$

The size distribution is described by a Gaussian function with a standard deviation σ_R. C is a normalization factor. $\mathcal{L}(q)$ is, for example, a Debye model with hard spheres (see [3]). The q-resolution is given by

$$\left(\frac{\Delta q}{q}\right)^2 = (\cot\theta \Delta\theta)^2 + \left(\frac{\Delta\lambda}{\lambda}\right)^2 \tag{19}$$

which is composed of an angular resolution term and a second wavelength resolution term.

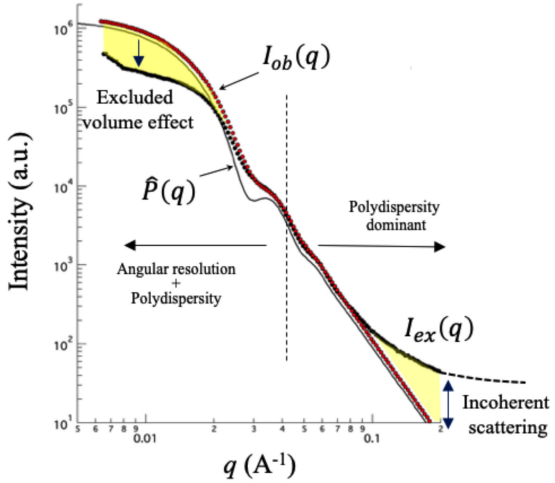

Figure 12. Scattering obtained for SiO_2 microsphere, for examining the q-resolution. $I_{ex}(q)$ (black symbol) is the scattering profile experimentally determined. $\hat{P}(q)$ is smeared by the size distribution of spheres given by Equation (23) and $I_{ob}(q)$ is smeared by both size distribution and instrument angular resolution. The broken line is a guide for the eye showing incoherent scattering.

In the low-q limit, the first term $(\cot\theta\Delta\theta)^2$ is dominant, whereas at high q, the second term $\Delta\lambda/\lambda$ is dominant (in case of iMATERIA, $\Delta\lambda/\lambda = 0.00043$). $\Delta\theta$ is the beam divergence of incident beam, which is determined by the combination of collimator slit widths S_1 and S_2 and the detector element size.

Next, we examined the q-resolution for the small-angle scattering bank ($0.5 < 2\theta < 5.5°$) and low-angle scattering bank ($20 < 2\theta < 40°$), which gives $q_{\max}/q_{\min} = 1333$.

The smeared scattering is given by

$$\hat{I}(q) = \int \mathcal{R}(t-q)\hat{P}(t)dt \tag{20}$$

$\hat{P}(q)$ is an analytical scattering function for a spherical object, after averaging over a size distribution. The resolution function is given by a gaussian function [35], as follows:

$$\mathcal{R}(t) = \frac{1}{(2\pi)^{1/2}\delta q}\exp\left[\frac{-(q-t)^2}{2(\delta q)^2}\right] \tag{21}$$

and

$$\delta q = \left[\frac{\delta\lambda}{\lambda} + cot\theta\ \delta\theta\right]q. \tag{22}$$

In case of time-of-flight (wavelength-dispersive method), we sum up the scattering functions with different wave lengths $\lambda_{max} > \lambda > \lambda_{min}$ which gives a certain range of q.

$$I_{ob}(q) = \sum_{\lambda_{min}}^{\lambda_{max}} \hat{I}(q) \tag{23}$$

Figure 12 shows the observed SANS $I_{ob}(q)$ and the analysis including the size distribution and q-resolution with $\delta\theta = 0.0025$ rad and $\delta\lambda/\lambda = 0.00043$, which is common for a powder diffractometer at pulsed source. Note that $I_{ex}(q)$ is the scattering profile experimentally determined. The size distribution was determined to be $R_{AV} = 160$ Å and $\sigma_R = 30$ Å. In the region $q > 0.04$ Å^{-1}, $I_{ob}(q)$ is smeared by the size distribution. For $q < 0.04$ Å^{-1}, $I_{ob}(q)$ is affected by the angular resolution of $\delta\theta = 0.0025$ rad, in addition to the size distribution. The discrepancy at low q may be due to inter-particle interference ($\mathcal{L}(q)$) or to excluded volume effects. The deviation at high q is due to incoherent scattering, which is

not included in the analytical model. The angular divergence of $\delta\theta$ = 0.0025 rad is determined by the supermirror tubes after the disk chopper; its length is 11.75 m and cross-section is 34 × 34 mm^2 gives $\delta\theta$ = 0.0028 rad.

5.2. Challenging Topics of Industrial Use

5.2.1. One-Shot Observation Covering a Wide Range of Length Scales (1 A~100 nm)

Figure 13a shows a scattering curve obtained for the polymer electrolyte Nafion®. Three sheets (each of thickness 50 μm) are packed in an aluminum holder, swollen by H_2O or D_2O, and dried. The small-angle detector covers a q-range of 0.007 < q <0.5 ($Å^{-1}$), whereas the low-angle detector covers a q-range of 0.2< q < 5 ($Å^{-1}$). The hierarchical self-assembled structure is recognized by the scattering maxima attributed to crystalline grains at q =0.055 $Å^{-1}$ (~20 nm), water channels or ion cluster at q = 0.15–0.2 $Å^{-1}$ (~nm) and crystalline chain order at q = 1.2 $Å^{-1}$. At higher q (>0.5 $Å^{-1}$), incoherent scattering from hydrogen in the films appears in proportion to its concentration. The result was obtained at a proton beam power of 200 kW, with double-frame operation (80-ms time interval). The measurement time was 600 s When at J-PARC's full beam power of 1 MW, with single frame operation, we expect this to reduce to 60 s We will then be able to detect a hierarchical structure or transient states, during processing.

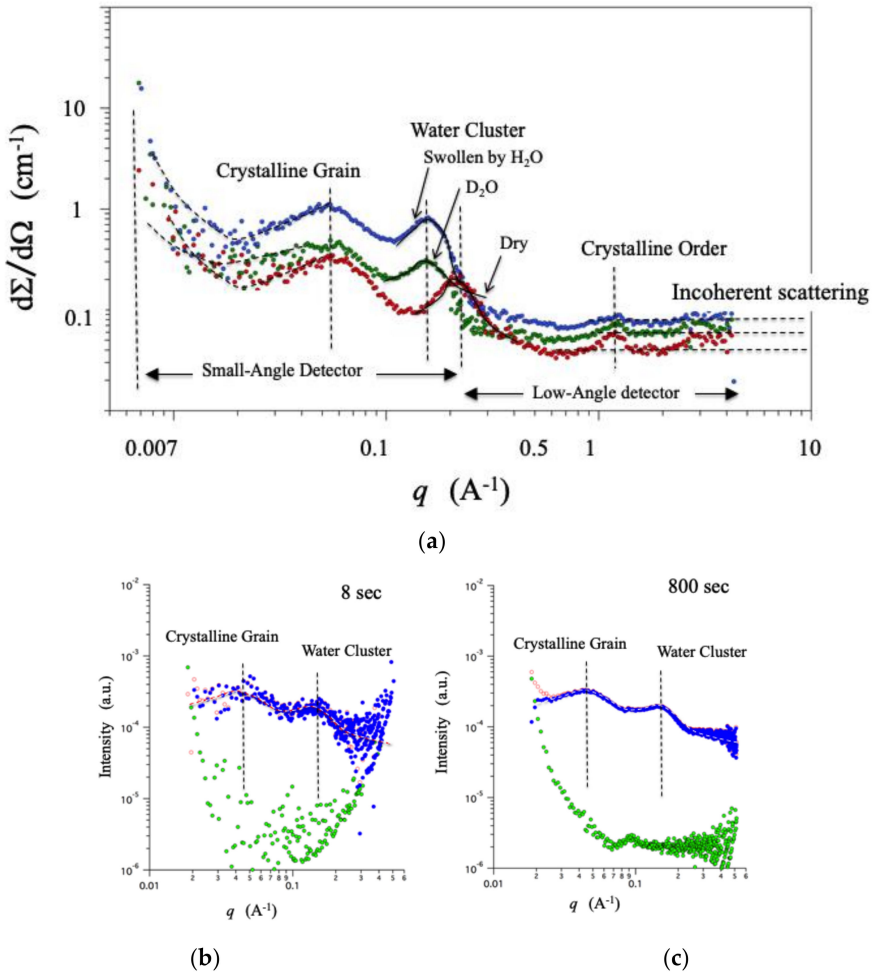

Figure 13. (**a**) Scattering profiles obtained for polymer thin film (Nafion®) at a dry state (red), or a swollen state with H_2O or D_2O (blue or green, respectively). (**b**,**c**) Time-dependent scattering obtained for thin film (Nafion®) (blue) and background (green) after histograms for 8 s and 800 s.

After performing the measurements, the user can generate histogram event data on a personal computer (part ① in Figure 6), in a flexible manner. Figure 13a,b demonstrate the results obtained by summing up different numbers of event data. Evaluation of an appropriate measurement time is as follows: for 8 s (100 flames), the profile exhibits large errors, whereas for 800 s (10,000 flames), the profile exhibits better statistics.

5.2.2. Time-Resolved and Wide Range of Length Scales: Vanishing Foam

In Figure 14, we report a time-resolved observation on a vanishing foam structure. A wide range of length scales (1 Å~100 nm) is covered by the single-shot measurement. The foam was prepared with an air pump, at 140 mm height from the liquid surface. Amino acid-type surfactant molecules (*N*-dodecanoyl-*N*-(2-hydroxyethyl)-*β*-alanine) were investigated (denoted as C_{12}-*β*Ala-C_2OH). We prepared surfactant solution with D_2O (100 mmol dm^{-3}). Figure 14 shows time-resolved SANS obtained for C_{12}-*β*Ala-C_2OH, after starting the pump (time interval is 1 min, with a 500 MW operation). From smaller q, we recognize small-angle scattering attributed to (1) single bimolecular layers with a disk shape, (2) micelles in a bimolecular layer and (3) incoherent scattering due to hydrogen atoms of surfactants. As the time proceeds, the SANS profile changes according to the arrows in Figure 2. We found the following:

(i) Immediately after pumping a scattering maxima at around q = 0.075 Å^{-1} appears, attributed to the micelles in the foam. The interdomain distance (~80 Å) is identical to that found in the surfactant solution before pumping.

(ii) In the lower q-region, at 300~360 s after pumping, crossover q-behavior from q^{-2} to q^{-4} appears at q_c = 0.023 Å^{-1}. From q_c, we estimated the thickness of foam as d = 270 Å (=2π/q_c).

(iii) At higher q, incoherent scattering appears and its intensity decreases as time proceeds. This is due to water drainage and its dropping under gravity.

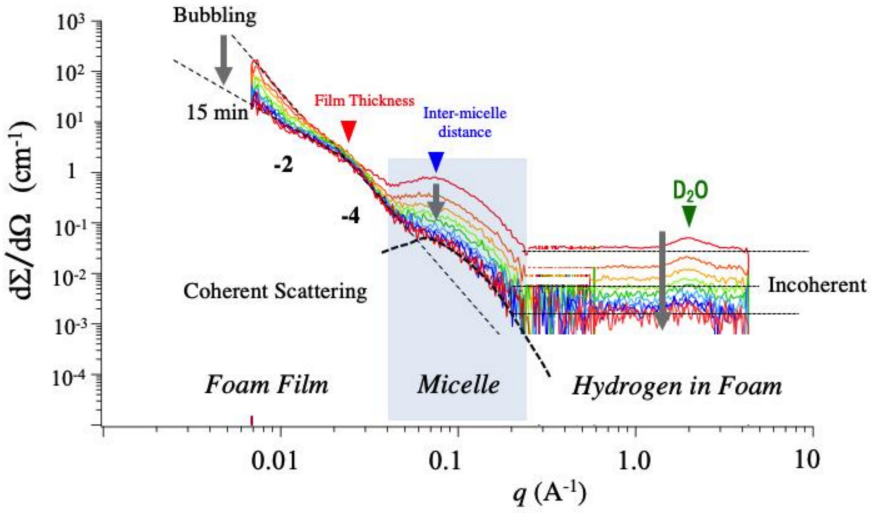

Figure 14. Time-resolved, small-angle scattering obtained for vanishing foam. Different colors indicate the scattering profiles obtained at different times between 1 and 15 min with a time interval 1 min.

The details of the date analysis are described in [36].

5.2.3. Fine Structure of Fuel Cell Catalyst, in Combination with Neutron Reflectivity

Normal SANS is performed with the incident beam along the z-axis, and we obtain $\vec{q} = (q_x, q_y, 0)$. By circularly averaging in q, carried out with the position of the direct neutrons as the origin, a SANS intensity $I(q)$ is acquired as a function of $q = \sqrt{q_x^2 + q_y^2}$. The powder of catalyst is packed in a plate-shape cuvette, i.e., an isotropic and spherically symmetric system (see Figure 15a). Random average on orientation in Θ gives the equation, the so-called Debye formalism in Equation (13).

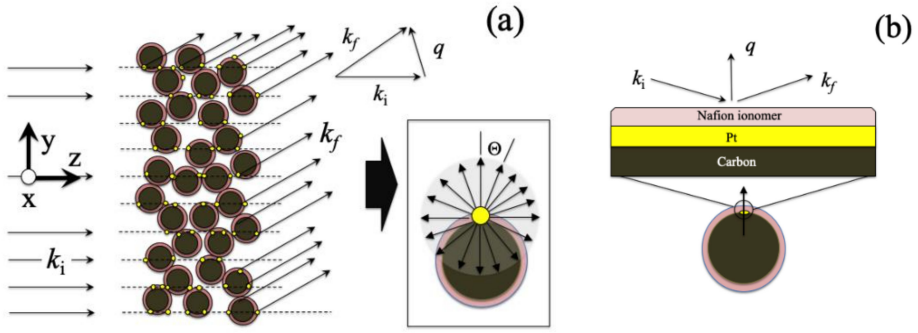

Figure 15. Schematic diagrams of (**a**) the normal powder catalyst and (**b**) the model system (for reflection geometry or in-situ grazing-incidence scattering (GISANS)) consisting of a spin-coated layer on a Si substrate.

By using contrast variation via water exchange with H_2O/D_2O, we observed SANS from the catalyst powder [37]. As a result of a model analysis using a core-shell structure, we determined an ionomer thickness of about 5 nm and that the water content is 17 wt.%. It should be denoted that the intra-layer structure of the Nafion® shell cannot be accessed by normal SANS. This is because of the random average on orientation in Θ and the Debye formalism.

To observe the local structure more clearly in the vicinity of the catalyst surface, we combine reflectivity measurements in order to reinforce the normal SANS. Reflectivity (specular reflection) is sensitive to the density profile (db/dz) along a direction of normal vector. Reflectivity is described by

$$R(q) \propto \frac{1}{q^4}\left|\int_{-\infty}^{\infty}\left(\frac{db}{dz}\right)e^{-izq}dz\right|^2 \tag{24}$$

To model the surface structure, Pt is sputtered onto a flat silicon substrate (111) and the Nafion® ionomer is spin-coated (see Figure 15a). Reflectivity was detected on iMATERIA using the reflection stages shown in Figure 9. As for the model catalysts prepared on Si substrate and humidified Nafion®, we determined layer thickness, water-thin layer on Pt surface, water distribution in a Nafion® thin layer and drying at surface. The details are given in [37].

5.2.4. Time-Resolved Total Reflection Measurement (Kinetic Measurement)

The time-of-flight wavelength-dispersive method enables us to perform time-resolved reflectivity within a short time interval, without having to move or rotate the sample. In order to determine mass transfer along the film thickness direction, we performed time-resolved total reflection measurements [31]. Figure 16a shows a schematic diagram of total reflection at the Fresnel surface between the bulk Nafion® film and Si substrate, as reported in [31]. After exchanging water from H_2O to D_2O, we can detect the change in total reflection angle at the Fresnel surface behind the film. Figure 16b shows the time-resolved total reflection for water exchange from D_2O to H_2O with a 5-min time interval. Obviously, the critical wave number for total reflection (q_c) shifts from high to low q, and the q-behaviors in reflectivity curves becomes more rounded, which is attributed to the imaginary part of scattering length (incoherent scattering from hydrogen) at the Fresnel interface. After analyses of the time-resolved reflectivity, we evaluated the diffusion coefficient of water in a Nafion® film swollen by water.

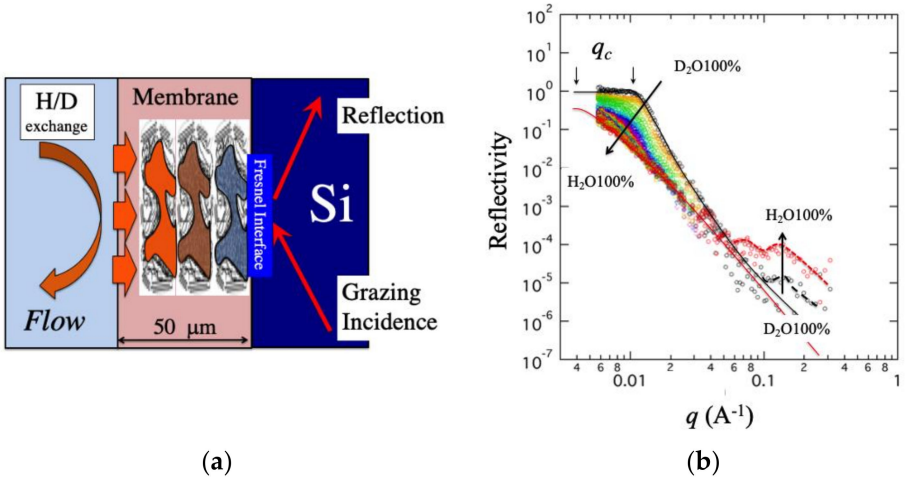

Figure 16. Schematic diagram showing (**a**) the Fresnel surface between Nafion® film and the silicon substrate, and (**b**) time-resolved total reflection during water exchange from D_2O to H_2O, in order to examine water diffusion across the bulk film. Different colors indicate the reflectivity (RF) profiles obtained at different times between 0 and 3 h with a time interval 5 min.

5.2.5. Spin Contrast Variation for Industrial Use

As mentioned in the introduction, DNP at the iMATERIA diffractometer is already opened for industrial uses: in [32], we report the first result obtained on the tire rubbers. For contrast variation, a deuteration method is normally used. One exchanges those hydrogen atoms bound to the molecule by covalent bonds, or one substitutes the solvent with a deuterated one. This method requires us to prepare a model system, simulating industrial products. It means that significant user effort and compromise are necessary. However, it is impossible to perform deuteration of the industrial goods themselves. To overcome this limitation, we have developed DNP apparatus for the iMATERIA diffractometer, with which we vary the coherent scattering length of hydrogen, by polarizing its nuclear spin via exchange with a paramagnetic center (radical) under extreme conditions of low temperature and high magnetic field. At low temperature 1.2 K and 7 tesla, the electron spin is 95% polarized at thermal equilibrium, whereas that of hydrogen is only 0.3%. This is because of the smaller nuclear magnetic moment. DNP is a technique to transfer the electronic spin state to the hydrogen nucleus using microwave irradiation [38]. For DNP, four technical requirements should be achieved, (1) high magnetic field, (2) low temperature, (3) microwave irradiation—all of which are facility efforts—and (4) radical doping of the sample, which will be a user effort.

Figure 17 shows the superconducting magnet with transverse magnetic field, up to 7 tesla and at 1.2 K, prepared for use on iMATERIA (BL20) [39]. The scattering angles of up to 20° are available for both forward and backward directions along the beam line, which corresponds to 50% of the total area of small-angle and low-angle detector banks. Note that the wavelength-dispersive TOF method overcomes this limitation because it scans q-value by wave length. Homogeneity in magnetic field is of order of 10^{-4} in the sample area (φ25 mm × 10 mm). The magnet is contained within a vacuum vessel (708 mm diameter) in order to set it in vacuum. It has 4 aluminum windows (0.5-mm thickness) to minimize parasitic scattering. The DNP apparatus is also available for powder diffraction. We change sample specimens using a top-loading stick, on the top of which we set two film specimens and the NMR pick-up coil is also allocated. With this magnet (7 tesla and 1.2 K), we successfully polarized the hydrogen nuclei of polystyrene to P_H = 95% [39].

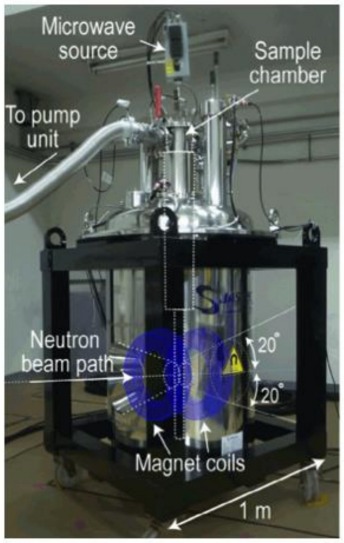

Figure 17. Superconducting magnet for dynamic nuclear polarization (DNP) on iMATERIA.

For multicomponent systems, the total small-angle scattering $I(q)$ is given by sum of individual partial scattering functions $S_{ij}(q)$,

$$I(q) = \sum_{i=0}^{P} \Delta b_i^2 S_{ii}(q) + 2 \sum_{i<j}^{P} \Delta b_{ij}^2 S_{ij}(q), \tag{25}$$

where the first and second terms are self- and cross-terms, respectively. Relative balance of partial scattering functions is determined by square of the difference in coherent scattering length density Δb^2. By performing contrast variation experiments with DNP, we obtain a series of SANS data for a single sample specimen. Then we solve the simultaneous equations to obtain the partial scattering functions.

The scattering length depends on polarizations for both neutron and nucleus (P_{N} and P_{H}).

$$\begin{array}{ll} b_{\mathrm{coh,H}} = -0.374 + 1.456\, P_{\mathrm{H}}\, P_{\mathrm{N}} & [10^{-12}\ \mathrm{cm}] \\ b_{\mathrm{coh,\,D}} = 0.667 & [10^{-12}\ \mathrm{cm}] \end{array} \tag{26}$$

where P_{N} and P_{H} are polarizations of the neutron and proton respectively. Both of P_{N} and P_{H} affect scattering length b. With $P_{\mathrm{H}} = 0$, which is the case of conventional contrast variation, using isotopic H and D, there is a large difference in b between hydrogen and deuterium. In the case of DNP, on the other hand, P_{H} is controlled so as not to equal to 0. DNP also controls incoherent scattering cross-section (Σ_{inc}),

$$\Sigma_{inc} = 1.54 \left(3 - 2P_N P_H - P_H^2\right) \left[\mathrm{cm}^{-1}\right] \tag{27}$$

For positive polarization $P_{\mathrm{H}} > 0$, Σ_{inc} decreases and at $P_{\mathrm{H}} = P_{\mathrm{N}} = 1$, it becomes zero. The decrease of Σ_{inc} may be useful for powder diffraction from organic crystalline materials.

We mentioned DNP for contrast variation is already open for industrial use at the iMATERIA diffractometer. The detailed analysis of DNP SANS on tire materials is described in [32]: a modern automobile tire is a multicomponent system including many additives (fillers of carbon black and SiO_2 particles, catalyst, all in a matrix of SBR rubber) in order to control roll resistance and stopping quality. The aim is to observe each of the bound rubber on the silica particles, the coupling agent and the tetrasulphide group near the surface selectively.

5.2.6. Perspectives for Completing the Multiscale Observation

In the empty space behind the SANS detector (position B in Figure 2), a USANS detector is installed in order to access $q_{min} = 10^{-4}$ Å^{-1}. Simultaneous scattering measurements using ultra-small-angle, small-angle, low-angle and backward detectors will achieve $q_{max}/q_{mix} = 10^6$, which covers the whole hierarchy shown in Figure 1. The pinholes, which shape the incident beam for small-angle scattering (2 θ~0 deg) and do not disturb the backward scattering (2θ~175 deg), have yet to be designed and installed. Powder diffraction (2θ~175 deg) will be measured on the specimens with a plate shape and included in our data reduction program in Figure 6. In the case of the TOF method, incoherent scattering from hydrogen, which is strongly affected by inelastic and multiple scattering, must be quantitatively subtracted. In addition, structural analysis in real space should be quantitatively combined with the SANS analysis [40]. The scattering contrast imaging [41,42] will be useful for industrial research, which is also our future work. Finally, the advanced SANS activities, for example, planned at the European spallation source (ESS) [43,44] will inspire researchers in the small-angle scattering community.

6. Conclusions

We have established SANS on the powder diffractometer iMATERIA, at BL20 of MLF, J-PARC. The multiscale from Ångstroms to 100 nm, which is described by $q_{max}/q_{mix} = 1000$, is covered simultaneously by combining the wavelength-dispersive and angle-dispersive methods. To extend applicable materials, we prepared the instrument options of neutron reflectivity and DNP for contrast variation, which are used for industry use.

Author Contributions: Conceptualization, S.K.; methodology, S.K.; software, H.I.; investigation, S.K., Y.N., T.M., T.I. and S.U.; resources, S.K.; writing—original draft preparation, S.K.; writing—review and editing, S.K., Y.N., R.A.R. and H.F.; supervision, S.K.; project administration, S.K.; funding acquisition, S.K., R.A.R. and H.F.; beam line advisors; T.F. User program. All authors have read and agreed to the published version of the manuscript.

Funding: The development of instrument was financially supported by Ibaraki Prefecture (Leading Research Project of Ibaraki Neutron Beam line). The work on fuel cell catalyst was supported by the Research and Development of Polymer Electrolyte Fuel Cell Technology project of the New Energy and Industrial Technology Development Organization (NEDO), Japan.

Acknowledgments: The authors thank, for technical advice, the chief engineers of Ibaraki prefecture government (Hironori Kodama, Makoto Hayashi and Toshiro Tomida) and the industrial use advisors of Ibaraki prefecture government (Yukio Morii and Toru Minemura). The authors also appreciate fruitful scientific discussions with Yukio Noda and Hideki Yoshizawa.

Conflicts of Interest: The authors declare no conflict of interest.

References and Note

1. Larson, R.G. *The Structure and Rheology of Complex Fluids*; Oxford University Press: Oxford, UK; New York, NY, USA, 1999.
2. Roland, C.M. *Encyclopedia of Analytical Chemistry*; John Wiley & Sons, Ltd.: Hoboken, NJ, USA, 2012. [CrossRef]
3. Imae, T.; Kanaya, T.; Furusawa, M.; Torikai, N. *Neutrons in Soft Matter*; Wiley: Hoboken, NJ, USA, 2011.
4. Koizumi, S.; Iwase, H.; Suzuki, J.; Oku, T.; Motokawa, R.; Sasao, H.; Tanaka, H.; Yamaguchi, D.; Shimizu, H.M.; Hashimoto, T. Focusing and polarized neutron small-angle scattering spectrometer (SANS-J-II). The challenge of observation over length scales from an angstrom to a micrometer. *J. Appl. Cryst.* **2007**, *40*, s474–s479. [CrossRef]
5. Eskildsen, M.R.; Gammel, P.L.; Issacs, E.D.; Detlefs, C.; Mortensen, K.; Bishop, D.J. Compound refractive optics for the imaging and focusing of low-energy neutrons. *Nature* **1998**, *391*, 563–566. [CrossRef]
6. Choi, S.-M.; Barker, J.G.; Glinka, C.J.; Cheng, Y.T.; Gammel, P.L. Focusing cold neutrons with multiple biconcave lenses for small—Angle neutron scattering. *J. Appl. Cryst.* **2000**, *33*, 793–796. [CrossRef]

7. Oku, T.; Iwase, H.; Shinohara, T.; Yamada, S.; Hirota, K.; Koizumi, S.; Suzuki, J.; Hashimoto, T.; Shimizu, H.M. A focusing-geometry small-angle neutron scattering instrument with a magnetic neutron lens. *J. Appl. Cryst.* **2007**, *40*, s408–s413. [CrossRef]
8. Bonse, U.; Hart, M. Tailless x-ray single-crystal reflection curves obtained by multiple reflection. *Appl. Phys. Lett.* **1965**, *7*, 238–240. [CrossRef]
9. Schwahn, D.; Miksovsky, A.; Rauch, H.; Seidl, E.; Zugarek, G. Test of channel-cut perfect crystals for neutron small angle scattering experiments. *Nucl. Instrum. Methods Phys. Res. Sect. A* **1985**, *239*, 229. [CrossRef]
10. Yamaguchi, D.; Koizumi, S.; Motokawa, R.; Kumada, T.; Aizawa, K.; Hashimoto, T. Tandem analyzer crystals system doubles counting rate for Bonse–Hart ultra-small-angle neutron-scattering spectrometer. *Phys. B Condens. Matter* **2006**, *385–386*, 1190–1193. [CrossRef]
11. Frielinghaus, H.; Pipich, V.; Radulescu, A.; Heiderich, M.; Hanslik, R.; Dahlhoff, K.; Iwase, H.; Koizumi, S.; Schwahn, D. Aspherical refractive lenses for small-angle neutron scattering. *J. Appl. Cryst.* **2009**, *42*, 681–690. [CrossRef]
12. Feoktystov, A.; Frielinghaus, H.; Di, Z.; Jaksch, S.; Pipich, V.; Appavou, M.-S.; Babcock, E.; Hanslik, R.; Engels, R.; Kemmerling, G.; et al. KWS-1 high-resolution small-angle neutron scattering instrument at JCNS: Current state. *J. Appl. Cryst.* **2015**, *48*, 61–70. [CrossRef]
13. Radulescu, A.; Pipich, V.; Frielinghaus, H.M.-S. KWS-2, the high intensity/wide Q-range small-angle neutron diffractometer for soft-matter and biology at FRM II 351 012026. *J. Phys. Conf. Ser.* **2012**, *351*, 012026. [CrossRef]
14. Wood, K.; Mata, J.; Garvey, C.J.; Wu, C.-M.; Hamilton, W.A.; Abbeywick, P.; Bartlett, D.; Bartsch, F.; Baxter, P.; Booth, N.; et al. QUOKKA, the pinhole small-angle neutron scattering instrument at the OPAL Research Reactor, Australia: Design, performance, operation and scientific highlights. *J. Appl. Cryst.* **2018**, *51*, 294–314. [CrossRef]
15. Okabe, S.; Karino, T.; Nagao, M.; Watanabe, S.; Shibayama, M. Current status of the 32 m small-angle neutron scattering instrument, SANS-U. *Nucl. Instrum. Methods Phys. Res. Sect. A Accel. Spectrometers Detect. Assoc. Equip.* **2007**, *572*, 853–858. [CrossRef]
16. Han, Y.-S.; Choi, S.-M.; Kim, T.-H.; Lee, C.-H.; Cho, S.-J.; Seong, B.-S. A new 40 m small angle neutron scattering instrument at HANARO, Korea. *Nucl. Instrum. Methods Phys. Res. Sect. A Accel. Spectrometers Detect. Assoc. Equip.* **2013**, *721*, 17–20. [CrossRef]
17. Masui, T.; Koizumi, S.; Hashimoto, T.; Shikinaka, K.; Kakugo, A.; Gong, J.P. Hierarchical structures of the actin/polycation complexes, investigated by ultra-small-angle neutron scattering and fluorescence microscopy. *Soft Matter* **2010**, *6*, 2021–2030. [CrossRef]
18. Koizumi, S.; Inoue, T. Dynamical coupling between stress and concentration fluctuations in a dynamically asymmetric polymer mixture, investigated by time-resolved small-angle neutron scattering combined with linear mechanical measurements. *Soft Matter* **2011**, *7*, 9248–9258. [CrossRef]
19. Koizumi, S.; Schwahn, D.; Annaka, M. Necklace-like microstructure in shallow-quenched aqueous solutions of poly(n-isopropylacrylamide), detected by advanced small-angle neutron scattering methods. *Soft Matter* **2019**, *15*, 671–682. [CrossRef]
20. Koizumi, S.; Zhao, Y.; Putra, A. Hierarchical structure of microbial cellulose and marvelous water uptake, investigated by combining neutron scattering instruments at research. *Polymer* **2019**, *176*, 244–255. [CrossRef]
21. Seeger, P.A.; Hjelm, R.P. JR Small-Angle Neutron Scattering at Pulsed Spallation Sources. *J. Appl. Cryst.* **1991**, *24*, 467–478. [CrossRef]
22. Heenan, R.K.; Penfold, J.; King, S.M. SANS at Pulsed Neutron Sources: Present and Future Prospects. *J. Appl. Cryst.* **1997**, *30*, 1140–1147. [CrossRef]
23. Dewhurst, C.D. D33—A third small-angle neutron scattering instrument at the Institute Laue Langevin. *Meas. Sci. Technol.* **2008**, *19*, 034007. [CrossRef]
24. Sokolova, A.; Whitten, A.E.; Campo, L.D.; Christoforidis, J.; Eltobaji, A.; Barnes, J.; Darmann, F.; Berry, A. Performance and characteristics of the BILBY time-of-flight small-angle neutron scattering instrument. *J. Appl. Cryst.* **2019**, *52*, 1–12. [CrossRef]
25. Carpenter, J.M.; Agamalian, M. Aiming for the theoretical limit of sensitivity of Bonse-Hart USANS instruments. *J. Phys. Conf. Ser.* **2010**, *251*, 012056. [CrossRef]
26. Agamalian, M.; Heroux, L.; Littrell, K.C.; Carpenter, J.M. Progress on The Time-of-Flight Ultra Small Angle Neutron Scattering Instrument at SNS. *IOP Conf. Ser. J. Phys. Conf. Ser.* **2018**, *1021*, 01203. [CrossRef]

27. Ikeda, Y.; Taketani, A.; Takamura, M.; Sunaga, H.; Kumagai, M.; Oba, Y.; Otake, Y.; Suzuki, H. Prospect for application of compact accelerator-based neutron source to neutron engineering diffraction. *Nucl. Instrum. Methods A* **2016**, *833*, 61–67. [CrossRef]
28. Koizumi, S.; Noda, Y.; Otake, Y.; Kobayashi, H. In preparation.
29. Noda, Y.; Izunome, H.; Maeda, T.; Inada, T.; Ueda, S.; Koizumi, S. The Large-Area Detector for Small-Angle Neutron Scattering on iMATERIA at J-PARC. *Quantum Beam Sci.* **2020**, *4*, 32. [CrossRef]
30. Ueda, S.; Koizumi, S.; Ohira, A.; Kuroda, S.; Frielinghaus, H. Grazing-incident neutron scattering to access catalyst for polymer electrolyte fuel cell. *Phys. B Condens. Matter* **2018**, *551*, 309–314. [CrossRef]
31. Koizumi, S.; Ueda, S.; Noda, Y. Time-resolved total reflection detects mass transfer along thickness direction of bulk Nafion® film. *Phys. B Condens. Matter* **2018**, *551*, 163–166. [CrossRef]
32. Noda, Y.; Maeda, T.; Oku, T.; Koizumi, S.; Masui, T.; Kishimoto, H. First Experiment of Spin Contrast Variation Small-Angle Neutron Scattering on the iMATERIA Instrument at J-PARC. *Quantum Beam Sci.* **2020**, *4*, 33. [CrossRef]
33. Ishigaki, T.; Hoshikawa, A.; Yonemura, M.; Morishima, T.; Kamiyama, T.; Tomiyasu, R.; Aizawa, K.; Sakuma, T.; Tomota, Y.; Arai, M.; et al. IBARAKI materials design diffractometer (iMATERIA)-Versatile neutron diffractometer at J-PARC. *Nucl. Instrum. Methods. A* **2009**, *600*, 189–191. [CrossRef]
34. Debye, P. Zerstreuung von Röntgenstrahlen. *Ann. Phys.* **1915**, *351*, 809–823. [CrossRef]
35. Pedersen, J.S.; Posselt, D.; Mortensen, K.J. Analytical treatment of the resolution function for small-angle scattering. *Appl. Cryst.* **1990**, *23*, 321–333. [CrossRef]
36. Koizumi, S.; Noda, Y.; Yada, S.; Yoshimura, T.; Fujita, H.; Shimosegawa, H.; Matsue, Y. Microscopic Depictions of Vanishing Shampoo Foam Examined by Time-of-flight Small-angle Neutron Scattering. (Under Review).
37. Koizumi, S.; Ueda, S.; Inada, T.; Noda, Y.; Robinson, R.A. Microstructure and water distribution in catalysts for polymer electrolyte fuel cells, elucidated by contrast variation small-angle neutron scattering. *J. Appl. Cryst.* **2019**, *52*, 791–799. [CrossRef]
38. Stuhrmann, H.B.; Brandt, B.; van den Hautle, P.; Konter, J.A.; Niinikoski, T.O.; Schmitt, M.; Willumeit, R.; Zhao, J.; Mango, S. Polarized neutron scattering from polarized nuclei near paramagnetic centers. *J. Appl. Cryst.* **1997**, *30*, 839–843. [CrossRef]
39. Noda, Y.; Koizumi, S. Dynamic nuclear polarization apparatus for contrast variation neutron scattering experiments on iMATERIA spectrometer at J-PARC. *Nucl. Instrum. Methods. A* **2019**, *923*, 127–133. [CrossRef]
40. Koizumi, S.; Ueda, S.; Nishikawa, Y.; Terao, T.; Kubo, N. New attempt to combine scanning electron microscopy and small-angle scattering in reciprocal space. *J. Appl. Cryst.* **2019**, *52*, 783–790. [CrossRef]
41. Liebi, M.; Georgiadis, M.; Menzel, A.; Schneider, P.; Kohlbrecher, J.; Bunk, O.; Guizar-Sicairos, M. Nanostructure surveys of macroscopic specimens by small-angle scattering tensor tomography. *Nature* **2015**, *527*, 349–352. [CrossRef]
42. Strobl, M.; Harti, R.P.; Grünzweig, C.; Woracek, R.; Plomp, J.J. Small Angle Scattering in Neutron Imaging. *Imaging* **2017**, *3*, 64. [CrossRef]
43. Frielinghaus, H. The European spallation source in a personal view for the German colloid and soft matter society. *Colloid Polym. Sci.* **2020**, *298*, 327–329. [CrossRef]
44. Andersen, K.H.; Argyriou, D.N.; Jackson, A.J.; Houston, J.; Henry, P.F.; Deen, P.P.; Toft-Petersen, R.; Beran, P.; Strobl, M.; Arnold, T.; et al. The instrument suite of the European Spallation Source. *Nucl. Instrum. Methods Phys. Res. A* **2020**, *957*, 163402. [CrossRef]